Drogue Dynamic Model Under Bow Wave in Probe-and-Drogue Refueling

ZI-BO WEI
XUNHUA DAI
QUAN QUAN
KAI-YUAN CAI
Beihang University
Beijing, China

Probe-and-drogue refueling (PDR) is widely adopted owing to its simple requirement of equipment and flexibility, but it has an apparent drawback that the drogue position is susceptible to disturbances. There are three types of disturbances: atmospheric turbulence, trailing vortex of the tanker, and bow wave effect caused by the receiver. The former two disturbances are independent of the receiver, whereas the bow wave effect, which depends on the state of the receiver, greatly influences the docking within a close distance. As far as the authors know, little attention has been paid to the bow wave effect on docking control in existing literature. The existing literature related to the bow wave focuses on either qualitative static results obtained from experiments, or lookup tables based on computational fluid dynamics (CFD) analysis. These are inapplicable to the PDR docking controller design directly. This paper proposes a lower order dynamic model to describe drogue dynamics under the bow wave effect. The model consists of two components: one is a second-order transfer function matrix to describe the drogue dynamics, and the other is a nonlinear function vector to describe the bow wave effect model. A closed-loop simulation including the two components shows that the generated drogue dynamics are similar to those of a real experiment reported in an existing literature.

Manuscript received December 2, 2014; revised August 19, 2015, November 8, 2015; released for publication February 17, 2016.

DOI. No. 10.1109/TAES.2016.140912.

Refereeing of this contribution was handled by I. Hwang.

This work was supported by the National Natural Science Foundation of China under Grant 61473012.

Authors' address: School of Automation Science and Electrical Engineering, Beihang University, New Main Building, E603, Beijing 100191. Corresponding author is Z.-B. Wei, E-mail: (whisper@buaa.edu.cn).

NOMENCLATURE

$o_i - x_i y_i z_i$	=	inertial frame with axes (x_i, y_i, z_i)
$o_t - x_t y_t z_t$	=	frame fixed to the conjunctive point between the tanker and the hose with axes (x_t, y_t, z_t)
$o_r - x_r y_r z_r$	=	frame fixed to the mass center of the receiver with axes (x_r, y_r, z_r)
$o_f - x_f y_f z_f$	=	frame fixed to the cockpit of the receiver with axes (x_f, y_f, z_f) and used in CFD software
$\boldsymbol{\theta}_{r/t}$	=	Euler angle vector describing the rotation from $o_t - x_t y_t z_t$ to $o_r - x_r y_r z_r$, deg
$\boldsymbol{\theta}_{r/i}$	=	Euler angle vector describing the rotation from $o_i - x_i y_i z_i$ to $o_r - x_r y_r z_r$, deg
$\boldsymbol{v}_t$	=	velocity vector of the tanker, m/s
v	=	refueling velocity, m/s
h	=	refueling altitude, m
L_j	=	the jth link
l_j	=	length of L_j, m
l_{dr}	=	length of the drogue, m
$\boldsymbol{p}_{L_j}$	=	position vector of the end of L_j, m
$\boldsymbol{p}_r$	=	position vector of the mass center of the receiver, m
$\boldsymbol{p}_d$	=	position vector of the center of the drogue canopy, m
$\boldsymbol{p}_p$	=	position vector of the probe's fore-end, m
$\boldsymbol{p}_f$	=	position vector of the origin of the CFD frame, m
$\boldsymbol{p}_n$	=	position vector of the nose's fore-end of the receiver, m
$\boldsymbol{f}_b$	=	force vector of the bow wave effect acting on the drogue, N
$\boldsymbol{f}_a$	=	force vector of atmospheric turbulence, N
$\boldsymbol{f}_v$	=	force vector of the trailing vortex of the tanker, N
R^2	=	coefficient of determination
α_j, β_j	=	orientation angles of L_j, deg
CFD	=	computational fluid dynamics
GBN	=	generalized binary noise
NASA	=	National Aeronautics and Space Administration
NATO	=	North Atlantic Treaty Organization
PDR	=	probe-and-drogue refueling

I. INTRODUCTION

Air-to-air refueling is an effective method of increasing the endurance and range of aircraft by refuelling them in flight [1]. In addition, by refueling, aircraft are able to carry their maximum payload without reducing their range [2]. There are two major aerial refueling systems in operation today: Boeing's "Flying Boom" system and Cobham's "Probe-and-Drogue" system [3]. The probe-and-drogue system is widely adopted owing to its simple requirement of equipment and flexibility. In the probe-and-drogue system, a tanker aircraft releases a flexible hose which terminates in a conical shaped drogue and trails behind the tanker aircraft [3]. A receiver aircraft is equipped with a probe protruding from its nose. The probe is required to dock into the drogue precisely to establish the contact for fuel transfer.

Compared with the flying boom system, the probe-and-drogue system has an apparent drawback: the drogue position is susceptible to disturbances. Probe and drogue refueling (PDR) is mainly subject to three types of disturbances: atmospheric turbulence, trailing vortex of the tanker, and bow wave effect. The former two disturbances are independent of the receiver, whereas the bow wave effect depends on the state of the receiver. These make docking very difficult. The bow wave effect should be taken into consideration when two aircraft are very close to each other [4]. In PDR, the phenomenon of the bow wave effect acting on the drogue is that the drogue will escape once the receiver is following the drogue at a close distance. This is a major difficulty of docking control by the probe-and-drogue system. In the ATP-56(B) issued by NATO [5], two rules are emphasized to deal with the bow wave effect during a PDR procedure: 1) a rapid approach should be avoided as it may cause the hose to whip and further a potential damage to the refueling equipment; 2) on the other hand, since a slow approach will make the drogue oscillate under the receiver's bow wave, the receiver pilot must resist a late attempt to capture. Compared with the rapid approach, the slow approach is much safer but with the control difficulty brought by the bow wave effect.

Many controller and machine vision sensors are designed for air-to-air refueling [6, 7], but little attention has been paid to the bow wave effect in existing literature on docking control. In [8], two types of flight test experiments were performed by NASA to study the area of influence (AOI) of the bow wave effect. In [9], another NASA flight test experiment was made to reveal the bow wave effect once capture was attempted. In [10], the bow wave effect of the receiver aircraft was incorporated into the hose and drogue model in terms of drag forces. Computational fluid dynamics (CFD) methods were used to generate a flow field solution for a nose similar to that of F-16 aircraft. In recent years, several papers on aerial refueling have been published in which the bow wave effect was discussed specifically. The bow wave in boom refueling was analyzed in [11], while the bow wave effect in PDR was modeled as a lookup table [3]. A trajectory of approaching the drogue in the complex flow field including bow wave has been analyzed in [12]. As mentioned above, existing literature related to the bow wave focus on either qualitative static results obtained from the experiments, or lookup tables based on CFD analysis. These are not directly applicable to the PDR docking controller design.

These considerations above motivate us to propose a lower order dynamic model to describe drogue dynamics under the bow wave effect. The model has two components: a drogue dynamic model and a bow wave effect model. In order to build the drogue dynamic model, the hose-drogue dynamic model [13] is established as a higher order link-connected system first. It is then simplified to be only a second-order linear drogue dynamic model at the reference equilibrium by parameter identification. On the other hand, in order to build the bow wave effect model, training data within the bow wave effect working area are first obtained by CFD software. Based on profiles of these training data, the bow wave effect is figured out in the form of a nonlinear function vector with undetermined parameters. Finally, based on these training data, the parameters are determined by nonlinear regression. The proposed dynamic model can 1) facilitate the PDR docking controller design and simulation, 2) facilitate the qualitative analysis of a drogue dynamics while a receiver is capturing the drogue.

This paper is distinguished from a conference paper in Chinese of ours [14], which proposed the drogue dynamic model. There are significant differences between the work presented in this paper and that presented in [14]: 1) the bow wave effect model is proposed additionally (Section IV); 2) a new and comprehensive simulation including the drogue dynamic model and bow wave effect model is performed and then compared with the experiment in [9] (Section V); 3) a part of the drogue dynamic model is rephrased in detail (Section II-A) including the reason to simplify the hose-drogue dynamic model (Section II-B).

II. PROBLEM FORMULATION

A. Frames and Notations

As shown in Fig. 1, in PDR, a tanker releases a flexible hose which terminates in a conical shaped drogue. A receiver aircraft is equipped with a probe protruding from its nose. In order to model drogue dynamics under the bow wave effect, four major frames are used in this paper: the inertial frame, the tanker frame, the receiver frame, and the CFD frame.

1) *Inertial frame* ($o_i - x_i y_i z_i$): This frame is a nonaccelerating flat Earth. The axis $o_i x_i$ is aligned with the projection of the velocity of the tanker on $x_i o_i y_i$ for convenience.

2) *Tanker frame* ($o_t - x_t y_t z_t$): The origin of the this frame is fixed to the conjunctive point between the tanker and the hose. The frame axes (x_t, y_t, z_t) are aligned with the wind frame forward-right-down directions of the tanker, namely the direction of $o_t x_t$ is identical with the velocity of the tanker $\boldsymbol{v}_t \in \mathbb{R}^3$.

3) *Receiver frame* ($o_r - x_r y_r z_r$): The origin of this frame is fixed to its mass center $\boldsymbol{p}_r$. The frame axes (x_r, y_r, z_r) are aligned with the body frame forward-right-down directions of the receiver.

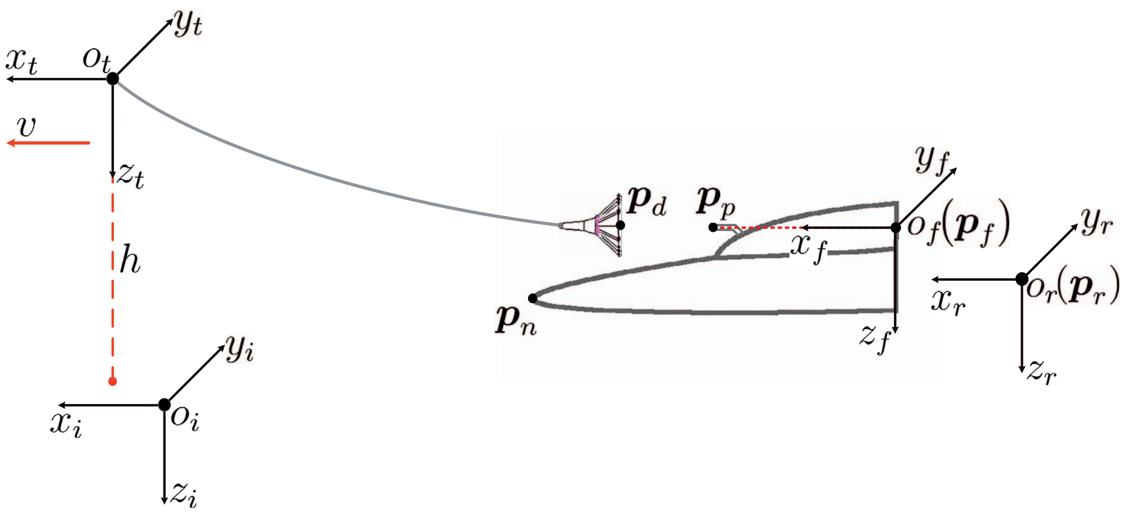

Fig. 1. Frames used in this paper.

4) *CFD frame* ($o_f - x_f y_f z_f$): The origin of this frame is fixed to the $x_r o_r z_r$ plane, and its height is the same as the probe. The frame axes (x_f, y_f, z_f) are aligned with the receiver frame. This frame described in detail in Section IV is used to model the bow wave effect force acting on the drogue.

In this paper, the rules of defining notations in [15] are followed.

1) A right subscript of a vector is used to designate two points for a position vector, or a point for a velocity, acceleration or force vector. A "/" in subscript will mean "with respect to."

2) A right superscript of a vector is used to specify a frame. It will therefore denote all elements of that vector in the specified frame.

3) The Euler angle vector between two frames is denoted by $\boldsymbol{\theta}_{\cdot/\cdot}$.

4) The elements of a position vector are denoted by x, y, z.

For example, $\boldsymbol{p}^i_{r/t} = [x^i_{r/t}, y^i_{r/t}, z^i_{r/t}]^{\mathrm{T}}$ denotes that the position vector of the receiver with respect to the tanker in the inertial frame, and $\boldsymbol{\theta}_{r/i}$ denotes the Euler angle vector of $o_r - x_r y_r z_r$ with respect to $o_i - x_i y_i z_i$, namely, it is the attitude angle vector of the receiver.

The following assumptions are made in this paper,

Assumption 1 $\boldsymbol{\theta}_{t/i} = \boldsymbol{\theta}_{r/t} = \boldsymbol{\theta}_{f/r} = 0$.

Assumption 2 $v \equiv v_0$, $h \equiv h_0$.

Remark 1 According to the definition of the frames mentioned above, $\boldsymbol{\theta}_{t/i} = \boldsymbol{\theta}_{f/r} = 0$. In addition, the receiver is assumed to keep a very small attitude angle to approach the drogue in the docking stage. Therefore, $o_r x_r$ is aligned with $\boldsymbol{v}_t$, which implies $\boldsymbol{\theta}_{r/t} = 0$. On the other hand, the refueling velocity and altitude are denoted by v, h, respectively. In general, $v = \|\boldsymbol{v}_t\|$. In the docking stage, since v, h change little compared with v_0, h_0, they are treated as constant parameters. Thus, assumption 2 is reasonable.

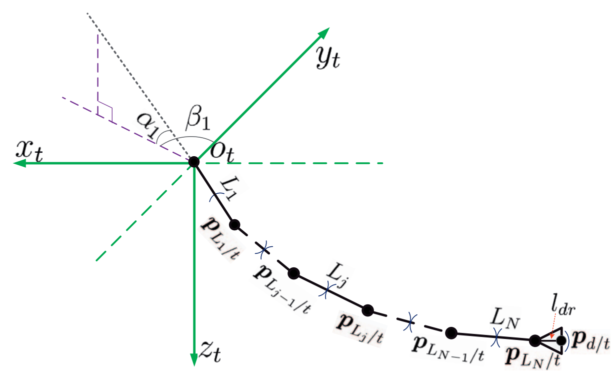

Fig. 2. Flexible hose-drogue dynamic model expressed by series of rigid links.

According to assumption 1, the orientations of the frames used in this paper are identical, so the superscripts of the notations are omitted and only the subscript is used to express the relative relation between two points. For example, since $\boldsymbol{p}^i_{r/t} = \boldsymbol{p}^t_{r/t} = \boldsymbol{p}^r_{r/t} = \boldsymbol{p}^f_{r/t}$, they are expressed as $\boldsymbol{p}_{r/t}$ uniformly by omitting their superscripts for convenience. The distance unit is meter, and the force unit is Newton. These units are omitted except in Section V for convenience. In order to compare our simulation results with the experiments in [9], feet is used in part of Section V.

B. Drogue Dynamic Model

A flexible hose-drogue dynamic model is often expressed by a series of rigid links according to the finite element method, which is called the link-connected model [13]. As shown in Fig. 2, the orientation of each link L_j with the length l_j is described by its orientation angles

$\alpha_j \in \mathbb{R}, \beta_j \in \mathbb{R}, j = 1, 2, \ldots, N$, where $N \in \mathbb{Z}^+$ is the number of rigid links. Then, each lumped mass position $\boldsymbol{p}_{L_j/t} \in \mathbb{R}^3$ and velocity $\dot{\boldsymbol{p}}_{L_j/t} \in \mathbb{R}^3$ are expressed by $\alpha_j, \beta_j, \dot{\alpha}_j, \dot{\beta}_j, l_j$.

Let $\boldsymbol{x} = [\boldsymbol{x}_1^{\mathrm{T}}, \boldsymbol{x}_2^{\mathrm{T}}, \ldots, \boldsymbol{x}_N^{\mathrm{T}}]^{\mathrm{T}} \in \mathbb{R}^{4N}$ and $\boldsymbol{x}_j = [\alpha_j, \beta_j, \dot{\alpha}_j, \dot{\beta}_j]^{\mathrm{T}} \in \mathbb{R}^4$. Then the hose-drogue dynamic model is expressed by

$$\begin{cases} \dot{\boldsymbol{x}}_h &= \mathbf{F}_{h0}\left(\boldsymbol{x}_h, \boldsymbol{x}_d, v, h, \boldsymbol{f}_a, \boldsymbol{f}_v\right) \\ \dot{\boldsymbol{x}}_d &= \mathbf{F}_{d0}\left(\boldsymbol{x}_h, \boldsymbol{x}_d, v, h, \boldsymbol{f}_a, \boldsymbol{f}_v, \boldsymbol{f}_b\right) \\ \boldsymbol{p}_{d/t} &= \mathbf{F}_y\left(\boldsymbol{x}_h, \boldsymbol{x}_d\right) \end{cases}, \tag{1}$$

where $\boldsymbol{x}_h = [\boldsymbol{x}_1^{\mathrm{T}}, \boldsymbol{x}_2^{\mathrm{T}}, \ldots, \boldsymbol{x}_{N-1}^{\mathrm{T}}]^{\mathrm{T}} \in \mathbb{R}^{4(N-1)}$ is the hose state and $\boldsymbol{x}_d = \boldsymbol{x}_N$ is the drogue state. As shown in Fig. 2, the drogue position is denoted by $\boldsymbol{p}_{d/t} = \boldsymbol{p}_{L_N/t} - [l_{dr}, 0, 0]^{\mathrm{T}}$, where l_{dr} is the length of the drogue. The external forces acting on the hose and drogue are $\boldsymbol{f}_a \in \mathbb{R}^3$, $\boldsymbol{f}_v \in \mathbb{R}^3$, $\boldsymbol{f}_b \in \mathbb{R}^3$, representing the atmospheric turbulence force, trailing vortex force of the tanker, and bow wave force caused by the receiver, respectively. Since $\boldsymbol{f}_b$ works only within a close range (a few meters) before the receiver nose, it is assumed to affect only the drogue. As far as the authors know, little attention has been paid on the bow wave effect $\boldsymbol{f}_b$, whereas the disturbances $\boldsymbol{f}_a$ and $\boldsymbol{f}_v$ have been studied extensively [16–20]. If the effect of $\boldsymbol{f}_a, \boldsymbol{f}_v$ on $\boldsymbol{p}_{d/t}$ are superposed with $\boldsymbol{f}_b$, then the final effect will be achieved. For simplicity, only the effect of $\boldsymbol{f}_b$ on $\boldsymbol{p}_{d/t}$ is taken into account here, leaving $\boldsymbol{f}_a = 0$ and $\boldsymbol{f}_v = 0$. Then, (1) is written as

$$\begin{cases} \dot{\boldsymbol{x}}_h &= \mathbf{F}_h\left(\boldsymbol{x}_h, \boldsymbol{x}_d\right) \\ \dot{\boldsymbol{x}}_d &= \mathbf{F}_d\left(\boldsymbol{x}_h, \boldsymbol{x}_d, \boldsymbol{f}_b\right) \\ \boldsymbol{p}_{d/t} &= \mathbf{F}_y\left(\boldsymbol{x}_h, \boldsymbol{x}_d\right) \end{cases}, \tag{2}$$

where $\mathbf{F}_h(\boldsymbol{x}_h, \boldsymbol{x}_d) \triangleq \mathbf{F}_{h0}(\boldsymbol{x}_h, \boldsymbol{x}_d, v_0, h_0, \mathbf{0}, \mathbf{0})$, $\mathbf{F}_d(\boldsymbol{x}_h, \boldsymbol{x}_d, \boldsymbol{f}_b) \triangleq \mathbf{F}_{d0}(\boldsymbol{x}_h, \boldsymbol{x}_d, v_0, h_0, \mathbf{0}, \mathbf{0}, \boldsymbol{f}_b)$. Under different flight conditions (v, h), the hose and the drogue have different steady states (when the hose-drogue device is not influenced by any disturbance, it will reach a steady position in the tanker frame, and the corresponding states in this position are the steady states). For a given flight condition (v_0, h_0), the steady states satisfy

$$\begin{cases} \dot{\boldsymbol{x}}_h^* &= \mathbf{F}_h\left(\boldsymbol{x}_h^*, \boldsymbol{x}_d^*\right) \\ \dot{\boldsymbol{x}}_d^* &= \mathbf{F}_d\left(\boldsymbol{x}_h^*, \boldsymbol{x}_d^*, \mathbf{0}\right) \\ \boldsymbol{p}_{d/t}^* &= \mathbf{F}_y\left(\boldsymbol{x}_h^*, \boldsymbol{x}_d^*\right) \end{cases}. \tag{3}$$

In order to analyze the major hose-drogue dynamics, a linear time-invariant system in the state-space form is obtained by linearizing the hose-drogue dynamic model (2) at the reference equilibrium condition $(\mathbf{x}_h = \mathbf{x}_h^*, \mathbf{x}_d = \mathbf{x}_d^*, \boldsymbol{f}_b = \mathbf{0})$ as follows,

$$\begin{cases} \begin{bmatrix} \Delta\dot{\boldsymbol{x}}_h \\ \Delta\dot{\boldsymbol{x}}_d \end{bmatrix} = \underbrace{\begin{bmatrix} \mathbf{A}_{11} & \mathbf{A}_{12} \\ \mathbf{A}_{21} & \mathbf{A}_{22} \end{bmatrix}}_{\mathbf{A}} \begin{bmatrix} \Delta\boldsymbol{x}_h \\ \Delta\boldsymbol{x}_d \end{bmatrix} \\ \quad + \underbrace{\begin{bmatrix} \mathbf{0} \\ \mathbf{B}_2 \end{bmatrix}}_{\mathbf{B}} \boldsymbol{f}_b \\ \quad + \begin{bmatrix} o\left(\Delta\boldsymbol{x}_h, \Delta\boldsymbol{x}_d\right) \\ o\left(\Delta\boldsymbol{x}_h, \Delta\boldsymbol{x}_d, \boldsymbol{f}_b\right) \end{bmatrix} \\ \Delta\boldsymbol{p}_{d/t} = \underbrace{\begin{bmatrix} \mathbf{C}_1 & \mathbf{C}_2 \end{bmatrix}}_{\mathbf{C}} \begin{bmatrix} \Delta\boldsymbol{x}_h \\ \Delta\boldsymbol{x}_d \end{bmatrix} \\ \quad + o\left(\Delta\boldsymbol{x}_h, \Delta\boldsymbol{x}_d\right) \end{cases}, \tag{4}$$

where

$$\begin{aligned} &\mathbf{A}_{11} = \left.\frac{\partial\mathbf{F}_h}{\partial\boldsymbol{x}_h}\right|_{\substack{\boldsymbol{x}_h=\boldsymbol{x}_h^* \\ \boldsymbol{x}_d=\boldsymbol{x}_d^*}}, \quad \mathbf{A}_{12} = \left.\frac{\partial\mathbf{F}_h}{\partial\boldsymbol{x}_d}\right|_{\substack{\boldsymbol{x}_h=\boldsymbol{x}_h^* \\ \boldsymbol{x}_d=\boldsymbol{x}_d^*}}, \\ &\mathbf{A}_{21} = \left.\frac{\partial\mathbf{F}_d}{\partial\boldsymbol{x}_h}\right|_{\substack{\boldsymbol{x}_h=\boldsymbol{x}_h^* \\ \boldsymbol{x}_d=\boldsymbol{x}_d^* \\ \boldsymbol{f}_b=\mathbf{0}}}, \quad \mathbf{A}_{22} = \left.\frac{\partial\mathbf{F}_{dr}}{\partial\boldsymbol{x}_d}\right|_{\substack{\boldsymbol{x}_h=\boldsymbol{x}_h^* \\ \boldsymbol{x}_d=\boldsymbol{x}_d^* \\ \boldsymbol{f}_b=\mathbf{0}}}, \\ &\mathbf{B}_2 = \left.\frac{\partial\mathbf{F}_d}{\partial\boldsymbol{f}_b}\right|_{\substack{\mathbf{x}_h=\mathbf{x}_h^* \\ \mathbf{x}_d=\mathbf{x}_d^* \\ \boldsymbol{f}_b=0}}, \\ &\mathbf{C}_1 = \left.\frac{\partial\mathbf{F}_y}{\partial\boldsymbol{x}_h}\right|_{\substack{\boldsymbol{x}_h=\boldsymbol{x}_h^* \\ \boldsymbol{x}_d=\boldsymbol{x}_d^*}}, \quad \mathbf{C}_2 = \left.\frac{\partial\mathbf{F}_y}{\partial\boldsymbol{x}_d}\right|_{\substack{\boldsymbol{x}_h=\boldsymbol{x}_h^* \\ \boldsymbol{x}_d=\boldsymbol{x}_d^*}}, \end{aligned} \tag{5}$$

and $\Delta\boldsymbol{p}_{d/t} = \boldsymbol{p}_{d/t} - \boldsymbol{p}_{d/t}^*$, $\Delta\boldsymbol{x}_h = \boldsymbol{x}_h - \boldsymbol{x}_h^*$, $\Delta\boldsymbol{x}_d = \boldsymbol{x}_d - \boldsymbol{x}_d^*$, and $o(\cdot)$ is the higher order term resulting from the linearization. By ignoring the higher order infinitesimal, (4) is a linear system. By the Laplace transform, the output vector $\Delta\boldsymbol{p}_{d/t}(s)$ is

$$\Delta\boldsymbol{p}_{d/t}(s) = \underbrace{\mathbf{C}(s\mathbf{I} - \mathbf{A})^{-1}\mathbf{B}}_{\mathbf{G}_d(s)} \boldsymbol{f}_b(s), \tag{6}$$

which is called the drogue dynamic model.

Many links are required to describe the flexible hose dynamics. Thus, the state space (4) is complex and not easy to obtain. So, $\mathbf{G}_d(s)$ in (6) is used to describe the drogue dynamics directly. For such a purpose, our objective is to establish an acceptable model for the drogue dynamics. Section III demonstrates the procedures in detail, and $\mathbf{G}_d(s)$ is approximated by a second-order transfer function matrix.

C. Bow Wave Effect Model

The bow wave effect is related to the relative position $\boldsymbol{p}_{d/r} \in \mathbb{R}^3$, relative velocity $\boldsymbol{v}_{d/r} \in \mathbb{R}^3$, and relative attitude $\boldsymbol{\theta}_{r/t} \in \mathbb{R}^3$. The receiver is supposed to adopt a slow approach to catch the drogue as emphasized in [3], namely $\|\boldsymbol{v}_{d/r}\| \approx 0$, so the contribution in the bow wave effect from $\boldsymbol{v}_{d/r}$ is ignored. Based on these considerations, $\boldsymbol{f}_b$ is taken as the following form

$$\boldsymbol{f}_b = \mathbf{R}\left(\boldsymbol{\theta}_{t/r}\right)\mathbf{F}_{b0}\left(\boldsymbol{p}_{d/r}, v, h\right), \tag{7}$$

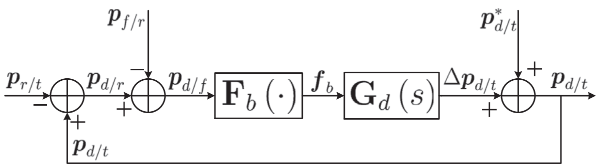

Fig. 3. Closed-loop simulation including $\mathbf{G}_d(s)$ and $\mathbf{F}_b(\cdot)$.

where $\mathbf{R}(\boldsymbol{\theta}_{t/r}) \in \mathbb{R}^{3\times3}$ is the rotation matrix from the receiver frame to the tanker frame. Since the aerodynamic force $\boldsymbol{f}_b$ is calculated by a CFD software, $\boldsymbol{p}_{d/r}$ is rewritten as

$$\boldsymbol{p}_{d/r} = \boldsymbol{p}_{d/f} + \boldsymbol{p}_{f/r}$$

where $\boldsymbol{p}_{d/f} \in \mathbb{R}^3$ is the drogue position with respect to the origin of the CFD frame $\boldsymbol{p}_f$. Consequently, (7) is replaced by

$$\boldsymbol{f}_b = \mathbf{R}\left(\boldsymbol{\theta}_{t/r}\right)\mathbf{F}_{b0}\left(\boldsymbol{p}_{d/f} + \boldsymbol{p}_{f/r}, v, h\right), \tag{8}$$

where $\boldsymbol{p}_{f/r} \in \mathbb{R}^3$ is a constant vector. Moreover, according to assumptions 1 and 2, (8) is simplified as

$$\boldsymbol{f}_b = \mathbf{F}_b\left(\boldsymbol{p}_{d/f}\right), \tag{9}$$

where $\mathbf{F}_b(\boldsymbol{p}_{d/f}) \triangleq \mathbf{F}_{b0}(\boldsymbol{p}_{d/f} + \boldsymbol{p}_{f/r}, v_0, h_0)$. Equation (9) is called the bow wave model.

Our objective is to establish the form of nonlinear function vector $\mathbf{F}_b(\cdot)$ with undetermined parameters first. The parameters are then estimated through training data from CFD software. Section IV demonstrates the procedures in detail.

D. The Outline of the Remainder Paper

The following sections are to build $\mathbf{G}_d(s)$ and $\mathbf{F}_b(\cdot)$ under $v = v_0$, $h = h_0$. The dynamic drogue position $\boldsymbol{p}_{d/t}$ driven by $\boldsymbol{f}_b$ is expressed by $\Delta\boldsymbol{p}_{d/t}(s) = \mathbf{G}_d(s)\boldsymbol{f}_b(s)$, while the relation between $\boldsymbol{f}_b$ and $\boldsymbol{p}_{d/r}$ is expressed by $\boldsymbol{f}_b = \mathbf{F}_b(\boldsymbol{p}_{d/f})$. The combination of the two models together can describe the drogue dynamics under the bow wave. In Section III, the link-connected model is established first to describe the hose-drogue dynamics. Then, system identification is employed to get the linear part of the link-connected model, namely the drogue dynamic model $\mathbf{G}_d(s)$. In Section IV, a CFD method is used to calculate the bow wave force acting on the drogue by setting the receiver and the drogue in different relative positions. The form of $\mathbf{F}_b(\cdot)$ is first inferred through the profiles of the training data. Then, parameters of $\mathbf{F}_b(\cdot)$ are further estimated by employing nonlinear regression. In Section V, as shown in Fig. 3, a closed-loop simulation including $\mathbf{G}_d(s)$ and $\mathbf{F}_b(\cdot)$ is established. It is used to simulate the drogue dynamics as a receiver approaches it. Then, the simulation results are compared with the experiment results from [9]. In Section VI, conclusions and the future works are reported.

III. SECOND-ORDER DROGUE DYNAMIC MODEL

The hose-drogue dynamics are described by a link-connected model in [13]. However, this model is too complicated to be used for controller design directly. Moreover, it also makes the simulation time consuming. In fact, in order to catch the drogue at a close distance, only the drogue dynamics are required to take into consideration in controller design, rather than the whole hose-drogue dynamics. According to this, the major drogue dynamics without the hose are modeled. The procedures to obtain the drogue dynamic model $\mathbf{G}_d(s)$ in (6) are shown in Table I. The simulation parameters are listed in Table II.

TABLE I
Procedures to Obtain the Drogue Dynamics $\mathbf{G}_d(s)$

Step 1:	Establish the hose-drogue dynamic model based on [13].
Step 2:	Infer the form of $\mathbf{G}_d(s)$ from the hose-drogue dynamic model by analyzing the drogue dynamics driven by selected disturbance forces.
Step 3:	Identify the parameters of $\mathbf{G}_d(s)$ from the hose-drogue dynamic model by using GBN.
Step 4:	Verify the identified model.

TABLE II
Simulation Parameters of Hose-Drogue Dynamic Model

Parameter	Value	Unit
Hose length	15	m
Hose radius	33.6	mm
Hose linear density	4.1	kg/m
Drogue weight	29.5	kg
Drogue radius	0.305	m
Refueling altitude h_0	3000	m
Refueling speed v_0	120	m/s

Step 1 is to obtain the hose-drogue dynamics. Steps 2–3 are to simplify the hose-drogue dynamics and obtain the drogue dynamic model. The realization and the reason to choose the form of $\mathbf{G}_d(s)$ are given in Appendix A in detail. By following the procedures in Table I, $\mathbf{G}_d(s)$ is obtained as follows

$$\Delta\boldsymbol{p}_{d/t}(s) = \underbrace{\begin{bmatrix} m_{11} & 0 & m_{13} \\ 0 & m_{22} & 0 \\ m_{31} & 0 & m_{33} \end{bmatrix}}_{\mathbf{G}_d(s)} \boldsymbol{f}_b(s), \tag{10}$$

where

$$\begin{aligned} m_{11} &= \frac{0.002185}{s^2 + 0.3071s + 2.682} \\ m_{13} &= \frac{0.006169}{s^2 + 0.3013s + 2.689} \\ m_{22} &= \frac{0.01712}{s^2 + 0.2422s + 2.081} \\ m_{31} &= \frac{0.005824}{s^2 + 0.3223s + 2.687} \\ m_{33} &= \frac{0.01782}{s^2 + 0.3391s + 2.687}. \end{aligned} \tag{11}$$

From (10), channel x is coupled with channel z, whereas channel y is independent because the corresponding

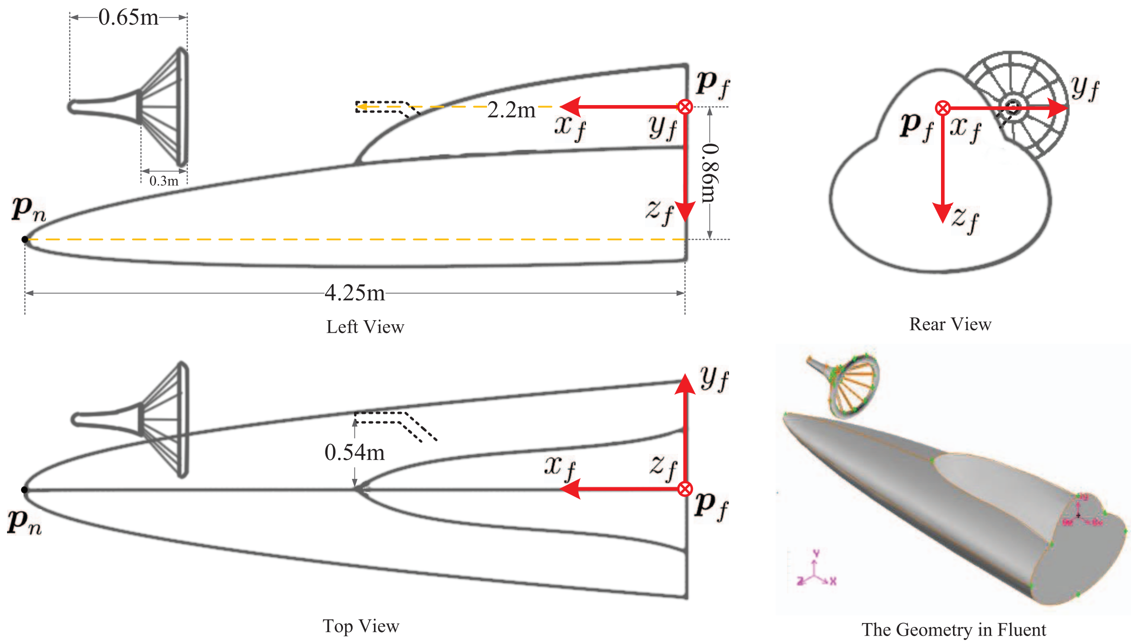

Fig. 4. Three views of drogue and receiver nose used in tests.

cross-terms in $\mathbf{G}_d(s)$ are zero. A chirp signal is employed to illustrate that the drogue dynamics generated by the simplified model (10) are close to those in the hose-drogue dynamics model (3) in the neighborhood of $\boldsymbol{p}^*_{d/t}$. The verification process is shown in Appendix A.

REMARK 2 The drogue dynamic model is simplified from the hose-drogue dynamic model and must sacrifice some accuracy. So, the drogue dynamic model is applicable to controller design, while the hose-drogue dynamic model is suitable for simulations.

IV. BOW WAVE EFFECT MODEL

According to (9), the bow wave effect model $\mathbf{F}_b(\cdot)$ is used to describe the relation between $\boldsymbol{f}_b$ and $\boldsymbol{p}_{d/f}$. In order to build $\mathbf{F}_b(\cdot)$, its form should be fixed first with undetermined parameters estimated sequentially by the training data acquired later from CFD software. The training data consists of the input data $\boldsymbol{p}_{d/f}$ and their corresponding output data $\boldsymbol{f}_b$. However, it is not easy to determine the form of $\mathbf{F}_b(\cdot)$ in theory as it depends on the structure and shape of the drogue, nose, and cockpit. On the other hand, it is not easy to infer the form of function $\mathbf{F}_b(\cdot)$ from the training data directly as the inputs $\boldsymbol{p}_{d/f}$ are three dimensional. In order to visualize $\mathbf{F}_b(\cdot)$, the profiles of the training data are employed to infer the form of $\mathbf{F}_b(\cdot)$. Finally, the parameters in $\mathbf{F}_b(\cdot)$ are optimized by nonlinear regression. The procedures are shown in Table III.

Fig. 4 shows the three views of drogue and the receiver nose used in the tests. Fig. 5 exhibits the geometry of the drogue. Since the objective of this paper is to analyze the main dynamics of bow wave rather than to obtain a precise model, the CFD calculations are simplified to some extent:

TABLE III
Procedures to Obtain the Bow Wave Effect Model $\mathbf{F}_b(\boldsymbol{p}_{d/f})$

Step 1:	Set up the CFD environment and establish the Fluent frame ($o_f - x_f y_f z_f$).
Step 2:	Generate training data whose inputs are from an area where the bow wave mainly works.
Step 3:	Infer the form of $\mathbf{F}_b(\cdot)$ based on the different profiles of the training data.
Step 4:	Estimate the parameters of $\mathbf{F}_b(\cdot)$ by applying nonlinear regression.
Step 5:	Check regression performance.

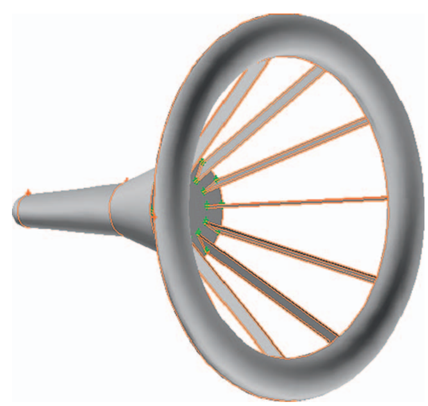

Fig. 5. Geometry of drogue.

1) the canopy is shaped as a solid circular ring without gore space on it; 2) the afterbody of the receiver is omitted including the wings, because the bow wave is mainly induced by the nose of the receiver, and the influence of the afterbody is much smaller. If a precise geometry of the drogue is needed, readers are suggested to refer to [21]. The fluid zone is similar to the deforming zone in [21] and

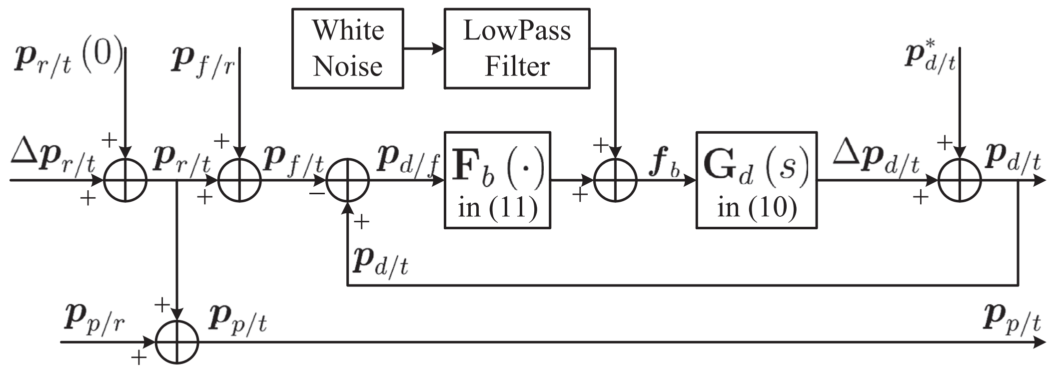

Fig. 6. Detailed structure of closed-loop simulation.

the detail of the computational setup is demonstrated in Appendix B. Set $v_0 = 120$, $h_0 = 3000$, which are the same as those in the simulation environment used in Section III. During the CFD calculations, the drogue and the forebody of the receiver are taken into consideration simultaneously, shown in Fig. 4.

By following the procedures in Table III, $\mathbf{F}_b(\cdot)$ is established as follows:

$$\mathbf{F}_b\left(\boldsymbol{p}_{d/f}\right) = \begin{bmatrix} f_{bx\_nose} + f_{bx\_cockpit} \\ f_{by} \\ f_{bz} \end{bmatrix}. \tag{12}$$

Here, $\boldsymbol{p}_{d/f} = [x_d,\ y_d,\ z_d]^{\mathrm{T}}$ and

$$\begin{cases} f_{bx\_nose} &= 91.6170\left[1 - 0.3220(x_d - 3.8870)^2\right] \\ &\quad \cdot e^{\frac{-y_d^2}{2.7395}} e^{\frac{z_d}{2.4838}} s\,(5.6493 - x_d) \\ f_{bx\_cockpit} &= 309.7709\,(1 - 0.3237x_d) \\ &\quad \cdot e^{\frac{-y_d^2}{0.3851}} e^{\frac{z_d}{1.1471}} s\,(3.0893 - x_d) \\ f_{by} &= 223.3210\,(1 - 0.2082x_d) \\ &\quad \cdot y_d e^{\frac{-y_d^2}{0.8102}} e^{\frac{z_d}{0.6555}} s\,(4.8031 - x_d) \\ f_{bz} &= -173.2021\,(1 - 0.2141x_d) \\ &\quad \cdot e^{\frac{-y_d^2}{0.5697}} e^{\frac{z_d}{0.7038}} s\,(4.6707 - x_d) \end{cases}. \tag{13}$$

where $s\,(x)$ is a step function as

$$s\,(x) = \begin{cases} 1 & \text{when } x \geqslant 0 \\ 0 & \text{when } x < 0 \end{cases}. \tag{14}$$

The choice of the form of $\mathbf{F}_b(\cdot)$ and the detailed procedures are given in Appendix B. From (13), the following conclusions are obtained: 1) f_{bx} is contributed by both the nose and the cockpit, denoted by f_{bx_nose} and $f_{bx\_cockpit}$, respectively; 2) these functions about y_d are either odd or even, because the nose is symmetry about $x_f o_f z_f$.

REMARK 3 The training data are confined to $(x_d,\ y_d,\ z_d) \in [2,\ 6] \times [-2,\ 2] \times [-0.5,\ 0.1]$ according to step 2 in Appendix B. Therefore, (13) describes the bow wave effect more accurately in this box and it still works in the neighborhood of the box. When $x_d > 6$, the bow wave does not influence the drogue actually, and $\mathbf{F}_b$ is zero in this case according to (13). Thus, (13) also fits the box $x_d > 6$. In the docking process, the bow wave effect mainly works in this box.

TABLE IV
Parameters Used in the Simulation Environment

h_0	=	3000	m
$p^*_{d/t}$	=	[0, 0, 0]	m
$p_{f/r}$	=	[3.86, 0, – 0.86]	m
v_0	=	120	m/s
$p_{r/t}$ (0)	=	[–12, –0.5, 0.86]	m
$p_{p/r}$	=	[6.06, 0.54, –0.86]	m
Noise Power of the White Noise = 1			
$Low\ Pass\ Filter = \frac{20}{20s+1}$			

V. NUMERICAL SIMULATION

In this section, to demonstrate the effectiveness, the model proposed in this paper is compared with the experiment in [9]. Reference [9] shows the first phase of the Autonomous Airborne Refueling Demonstration (AARD) project completed on August 30, 2006, where 6 docking experiments were performed.

A. Simulation Setting

The experimental details are not provided by [9]. Therefore, some unknown parameters of the experiment are assumed in the simulation. The structure of the simulation is shown in Fig. 6, where $\boldsymbol{p}_{r/t}(0) \in \mathbb{R}^3$ is the initial position of the receiver, and the band-limited white noise block and the low filter block are employed to simulate the atmospheric turbulence. For convenience, the origin of the tanker frame o_t is moved to the steady position of the drogue $\boldsymbol{p}^*_{d/t}$, namely, $\boldsymbol{p}^*_{d/t} = [0, 0, 0]^{\mathrm{T}}$. The parameters used in this simulation are shown in Table IV. The relative position between the receiver and the tanker is calculated by $\boldsymbol{p}_{r/t}(t) = \boldsymbol{p}_{r/t}(0) + \Delta\boldsymbol{p}_{r/t}(t)$, where $\Delta\boldsymbol{p}_{r/t}(t)$ is a trajectory with respect to the initial position of the receiver $\boldsymbol{p}_{r/t}(0)$. The probe is set to align with the drogue,

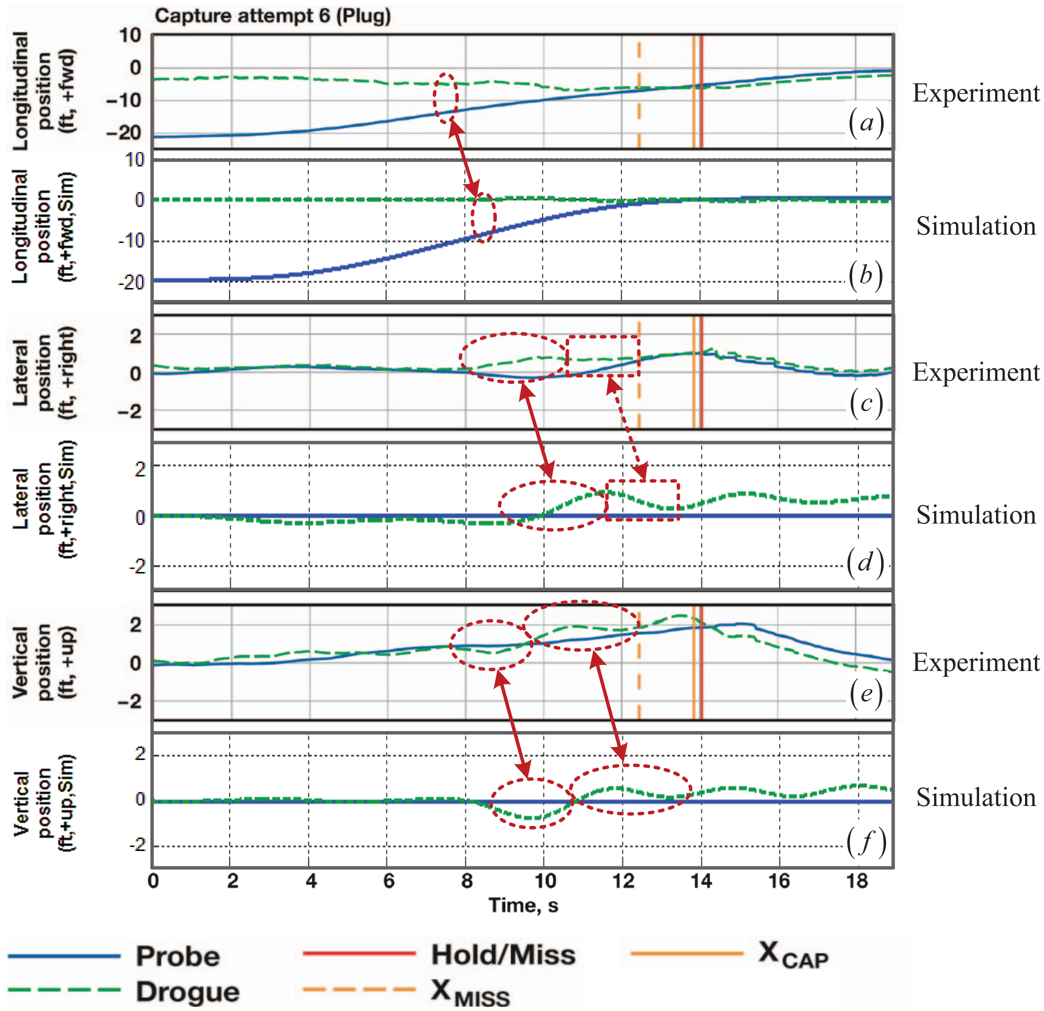

Fig. 7. Comparison between our simulation with experiment in [9]. (Symbol X_{MISS} means longitudinal distance that probe touches plane of canopy of drogue and X_{CAP} means longitudinal distance that probe captures drogue. Vertical position used here is height, which is equal to $-z_d$.)

so $\boldsymbol{p}_{r/t}(0)$ is chosen as $[-12, -0.54, 0.86]^{\mathrm{T}}$. Then, let the receiver approach the drogue directly, which means there is no movement in the $y_t o_t z_t$ plane, so $\Delta \boldsymbol{p}_{r/t} = [\Delta x_{r/t}, 0, 0]^{\mathrm{T}}$, where $\Delta x_{r/t}$ is set as follows:

$$\Delta \ddot{x}_{r/t}(t) = \begin{cases} 0 & \text{when } t = 0,\ t > 16 \\ 0.047 & \text{when } 0 < t \leqslant 4, \\ & \qquad 12 < t \leqslant 16 \\ -0.047 & \text{when } 4 < t \leqslant 12 \end{cases} . \qquad (15)$$
$$\Delta x_{r/t}(0) = 0$$

The purpose of choosing this trajectory is to make the trajectory of probe in the simulation similar to the experiment in [9] (see Fig. 7).

B. Simulation Results

One of the experiments in [9] is used to compare with the simulation results in this paper. To compare with [9], the distance unit is converted into feet (ft) in Fig. 7. Fig. 7 (a), (c), (e) are from [9], while Fig. 7 (b), (d), (f) are our simulation results. The corresponding video is available in [22], and the screenshot is shown in Fig. 8. As shown in the dash lines of Fig. 7, the drogue dynamics in the simulation are similar to those in the experiment. Concretely, some conclusions are summarized as follows.

1) As shown in Fig. 7, during $0 \sim 8$ s, the drogue is not influenced by the bow wave effect when the receiver nose is far from it.

2) As shown in Fig. 7 (e) and (f), during $8 \sim 10$ s, the drogue drops from its steady position when the receiver nose is close to it.

3) As shown in Fig. 7 (c), (d), (e), (f), during $10 \sim t_{X_{MISS}}$, the drogue drifts upward and right at the same time as the receiver nose passes it, where $t_{X_{MISS}}$ is the moment when the distance between the probe and drogue is X_{MISS} in the experiment.

4) The drogue dynamics have the property of second-order dynamics, so the three-dimensional trajectory of the drogue will be a helix in the final stage. In other words, the drogue will have a back swing if the receiver cannot catch the drogue. Furthermore, if the

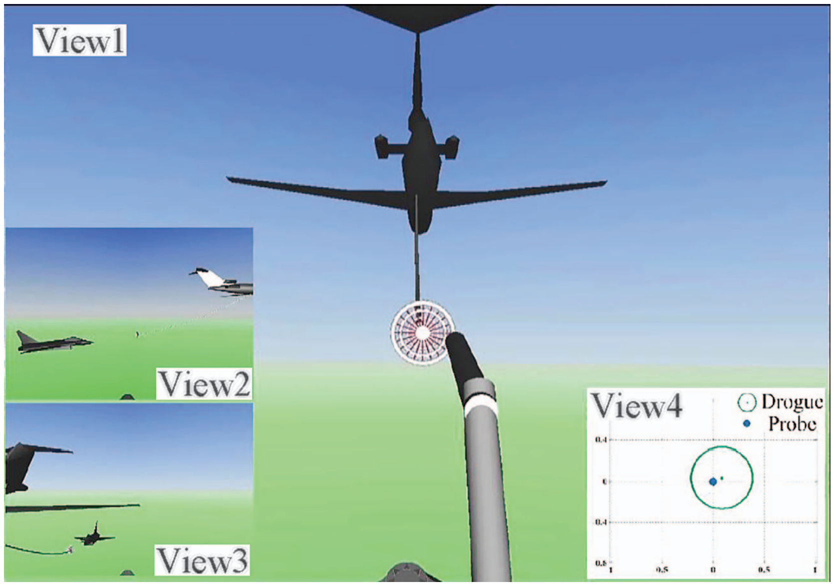

Fig. 8. Screenshot of video (view1 is from pilot view, view 2 is from side view, view 3 is from tanker view, while view 4 shows relation between probe and drogue in $x_t o_t y_t$).

receiver does not draw back immediately, then the drogue will have a back swing and may knock the receiver.

REMARK 4 After $t_{X_{MISS}}$, the receiver has touched the drogue in the experiment. Thus, this part is unavailable for comparison. Before $t_{X_{MISS}}$, there are still some small differences between the experiment and our simulation. The reasons are listed as follows.

1) The environments and the parameters (for example the shape of nose of the receiver, the relative position of the drogue with respect to the receiver, and so on) of the simulation and the experiment are not the same, because the experimental details are not provided by [9]. Moreover, because there is not a feedback docking controller designed in our simulation, unlike the trajectories in the experiment, the trajectory of the probe does not approach that of the drogue.

2) There are time shifts between the experiment and the simulation on the trajectories of the lateral position and the vertical position as Fig. 7 (c), (d), (e), (f) show, because the receiver in the experiment approached the drogue earlier as Fig. 7 (a) and (b) show.

3) The drop of vertical position of the simulation is lower than the experiment (in the left dash lines of Fig. 7 (e) and (f)). It is caused by f_{bx_nose} whose scope is within 5.5749 as (13) shows. However, there is a hose-drum unit (HDU) at the front end of the hose in the actual refueling [10]. It retracts the hose when the hose tension drops, which is mainly caused by the longitudinal force. This implies that the effect of f_{bx_nose} is weakened by the HDU. As a result, the drop is not remarkable in the experiment, while the raise is in turn more remarkable correspondingly.

4) As shown in the dashed rectangle box of Fig. 7 (c) and (d), the lateral positions are different. This will be explained in the following. In the experiment, a feedback docking controller attempts to make the probe and drogue align. As a result, as the receiver is close to the drogue, the trajectory of the drogue does not drop down. On the other hand, in our simulation, there is not a feedback docking controller, so when the bow wave starts to work, the receiver does not approach the drogue in the lateral direction. Thus, the trajectory of the drogue drops down after the climbing up in the dashed elliptical box. From them, the behavior in the experiment is also consistent with the proposed model, although the curves in the dashed rectangle box are different.

VI. CONCLUSION AND FUTURE WORK

It is very important to consider the bow wave effect for successful aerial refueling. This paper employs the "mechanism modeling + system identification" method to obtain the drogue dynamic model in the form of a transfer function matrix, and employs the "CFD + nonlinear regression" method to obtain the bow wave effect model in the form of a nonlinear function vector. The resulting drogue dynamics under bow wave effect in probe-and-drogue aerial refueling is similar to those in a real experiment. The contributions of the proposed model and method are: 1) the proposed model is applicable to a docking controller design to overcome the bow wave effect actively; 2) the proposed model can describe the drogue dynamics during the docking stage; 3) the proposed model can reduce the workload of wind tunnel experiments or real experiments to build a better bow wave effect model.

Future work will include:

1) The PDR docking controller for the receiver will be designed based on the proposed model.

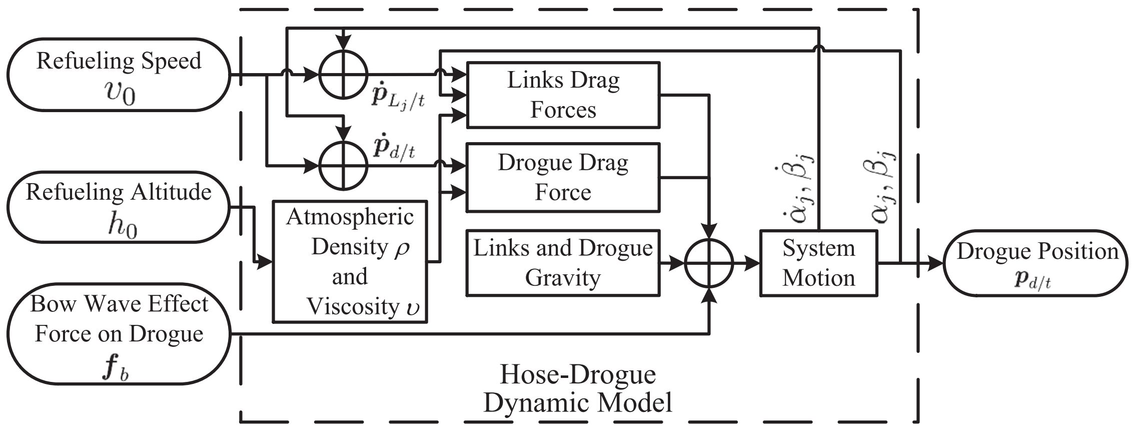

Fig. 9. Structure of hose-drogue dynamic model [14].

2) The quantitative relation between the parameters in the bow wave effect model and the shape of the receiver nose will be further analyzed.
3) The effect of HDU will be involved in the model.

APPENDIX A. DETAILED PROCEDURES OF TABLE I TO ESTABLISH $\mathbf{G}_d(s)$

Steps 1–4 have been finished in our previous work [14] in Chinese. In order to make this paper self-contained, the main process and results in [14] are also presented.

Step 1. *Establish the hose-drogue dynamic model:* The hose-drogue dynamics are described by a link-connected model in [13], where the hose is modeled by a series of ball-and-socket connected rigid links. Each link is subject to gravitational and fluid dynamic loads. The link masses and all external forces are lumped at the connecting joints, as shown in Fig. 2. The position of the hose and the drogue are described by a set of orientation angles measured relative to the tanker frame. Each lumped mass position $\boldsymbol{p}_{L_j/t}$ is expressed by two angles $\alpha_j,\ \beta_j$ and the length l_j of the link. The structure of the hose-drogue dynamic model is shown in Fig. 9, where the dashed box represents the dynamic system (2). Readers are suggested to refer to [13, 23] for details. This model is used to derive a simplified model which is as (16) shows, and to verify the effect of the simplification in step 4.

Step 2. *Infer the form of* $\mathbf{G}_d(s)$*:* Five simulations are executed, and the inputs $\boldsymbol{f}_b$ of them are set as $\boldsymbol{f}_{x+},\ \boldsymbol{f}_{y+},\ \boldsymbol{f}_{y-},\ \boldsymbol{f}_{z+},\ \boldsymbol{f}_{z-} \in \mathbb{R}^3$ respectively, where $\boldsymbol{f}_{x+} = [50, 0, 0]^{\mathrm{T}}, \boldsymbol{f}_{y+} = [0, 50, 0]^{\mathrm{T}}, \boldsymbol{f}_{y-} = [0, -50, 0]^{\mathrm{T}}$, $\boldsymbol{f}_{z+} = [0, 0, 50]^{\mathrm{T}}$, and $\boldsymbol{f}_{z-} = [0, 0, -50]^{\mathrm{T}}$. These axial forces are used to stimulate the system (2) to confirm the coupling in $\mathbf{G}_d(s)$. As shown in Table V, the drogue's max drift position $\Delta(\cdot)_{max}$ and the final drift position $\Delta(\cdot)_{final}$ with respect to the steady position are recorded. According to Table V, the following conclusions are made: 1) channel x is coupled with channel z; 2) channel y is regarded as an independent channel, because the effects caused by $\boldsymbol{f}_{y+}$ and $\boldsymbol{f}_{y-}$ on $\Delta x_{d/t}$ and $\Delta z_{d/t}$ are much smaller than those by $\boldsymbol{f}_{x+}, \boldsymbol{f}_{z+}, \boldsymbol{f}_{z-}$. Therefore, $\mathbf{G}_d(s)$ in (6) has the following simple form:

TABLE V
Drogue Drift Position Caused by $\boldsymbol{f}_b$ from Different Direction

$\boldsymbol{f}_b$	$\boldsymbol{f}_{x+}$	$\boldsymbol{f}_{y+}$	$\boldsymbol{f}_{y-}$	$\boldsymbol{f}_{z+}$	$\boldsymbol{f}_{z-}$
$\Delta(x_{d/t})_{max}$	0.070	0.015	0.015	0.204	0.177
$\Delta(x_{d/t})_{final}$	0.040	0.005	0.005	0.109	0.105
$\Delta(y_{d/t})_{max}$	0	0.724	−0.724	0	0
$\Delta(y_{d/t})_{final}$	0	0.410	−0.410	0	0
$\Delta(z_{d/t})_{max}$	0.199	−0.012	−0.012	0.560	−0.588
$\Delta(z_{d/t})_{final}$	0.115	−0.004	−0.004	0.324	−0.337

$$\Delta \boldsymbol{p}_{d/t}(s) = \begin{bmatrix} G_{xx}(s) & 0 & G_{xz}(s) \\ 0 & G_{yy}(s) & 0 \\ G_{zx}(s) & 0 & G_{zz}(s) \end{bmatrix} \boldsymbol{f}_b(s). \quad (16)$$

Step 3. *Identify the parameters of* $\mathbf{G}_d(s)$*:* GBN is taken as input to stimulate the hose-drogue dynamic model. Output-error (OE) model [24] is employed to identify the parameters of $\mathbf{G}_d(s)$. The model is shown as in (10).

Step 4. *Verify the identified model:* In order to verify the identified model, a chirp signal is selected as the input signal to stimulate both the identified drogue dynamic model $\mathbf{G}_d(s)$ and the original system (2) at the same time, as shown in Fig. 10. The chirp signal is given by

$$c(t) = 50 \sin\left[2\pi\left(f_0 + \frac{f_T - f_0}{T}t\right)t\right] \quad (17)$$

where $f_0 = 0.05, f_T = 0.5, T = 200$. As shown in Fig. 11, the drogue dynamics generated by the identified drogue dynamic model $\mathbf{G}_d(s)$ in (10) is similar to the those of the hose-drogue dynamic model (2) in the low frequency band.

APPENDIX B. DETAILED PROCEDURES OF TABLE III TO ESTABLISH $\mathbf{F}_b(\cdot)$

Step 1. *Setup CFD environment and establish the CFD frame* ($o_f - x_f y_f z_f$)*:* Two 3D geometric models of the forebody of the receiver and the drogue are built in

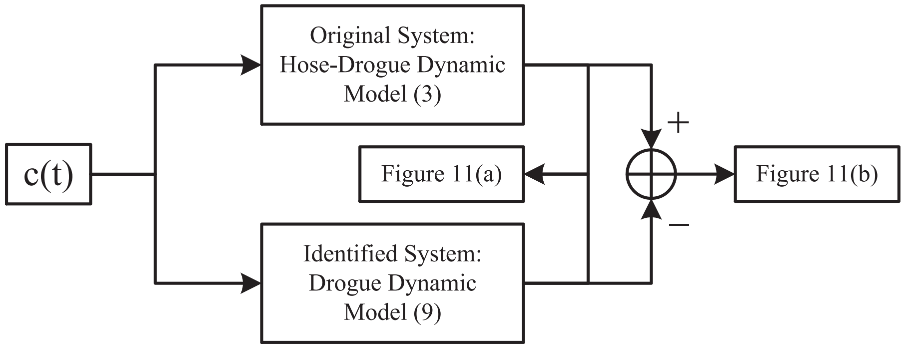

Fig. 10. Verification test of identified system.

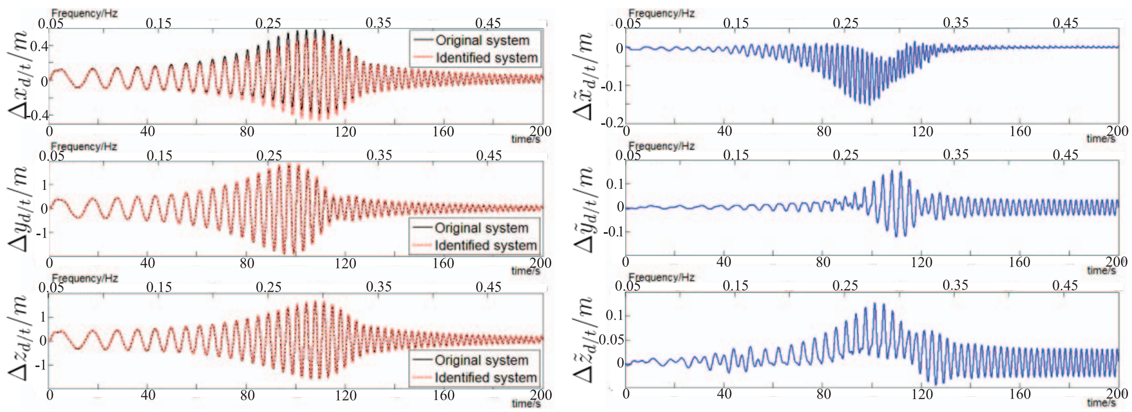

(a) Response of the sweep signal

(b) Error of the sweep signal

Fig. 11. Performance of system identification [14].

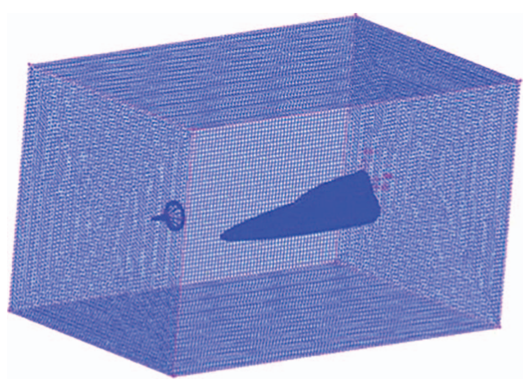

Fig. 12. Grid of cuboid zone.

Gambit as shown in Figs. 5 and 4. The computational domain is a cuboid zone with the size of 10 × 6 × 6, and the mesh used has about 2.6 million mixed cells, as shown in Fig. 12. To achieve a higher density, the grid with length about 0.005 is used around the surface of the drogue. The grid length is 20 times smaller than that near the boundary region. A standard k-epsilon model is used for the air viscous model and the pressure based formulation with implicit algorithm for the solver. Under this setting, the pressure on the drogue is acquired by using the commercial software Fluent.

Then, establish the CFD frame $o_f - x_f y_f z_f$ for the CFD tests. In this paper, Fluent is chosen as the CFD software. As shown in Fig. 1, the CFD reference point $\boldsymbol{p}_f$ is fixed in $x_r o_r z_r$, and $\boldsymbol{p}_f$ with respect to receiver position $\boldsymbol{p}_r$ is denoted by $\boldsymbol{p}_{f/r} = [x_{f/r}, y_{f/r}, z_{f/r}]^{\mathrm{T}}$. Choose $x_{f/r} = x_{p/r} - 2.2$, $y_{f/r} = 0$, $z_{f/r} = z_{p/r}$, where $\boldsymbol{p}_{p/r} = [x_{p/r},\ y_{p/r},\ z_{p/r}]^{\mathrm{T}} \in \mathbb{R}^3$ is the probe position with respect to $\boldsymbol{p}_r$. The reasons to choose such a $\boldsymbol{p}_{f/r}$ are: 1) $x_{f/r}$ is at the position of the cockpit, shown in Fig. 1; 2) since $y_{f/r} = 0$, the element of $\mathbf{F}_b\ (\boldsymbol{p}_{d/f})$ will be either an odd or an even function about $y_{d/f}$ thanks to the symmetry of the nose; 3) since $z_{f/r} = z_{p/r}$, the probe aligns with the drogue. Let $\boldsymbol{p}_f$ be the original point o_f of the coordinate system in the tests. In the remainder part of this section, all related variables are defined in the CFD frame. Therefore, for convenience, the subscript f of the variables measured in $o_f - x_f y_f z_f$ is omitted. For example, $\boldsymbol{p}_d = \boldsymbol{p}_{d/f}$, $x_d = x_{d/f}$, and $xoy = x_f\ o_f y_f$, etc.

Step 2. *Choose training data:* Training data are the pairs $(\boldsymbol{p}_{d,k}, \boldsymbol{f}_{b,k})$, where $k \in \mathbb{Z}^+$. Over two hundred training data are chosen in $\boldsymbol{p}_d \in [2, 6] \times [-2, 2] \times [-0.5, 0.1]$, where the bow wave effect mainly works. (The data are available in [25].) For example, when $\boldsymbol{p}_d = [3.5, 0, 0]^{\mathrm{T}}$, the contours of velocity magnitude are as shown in Fig. 13. Fluent can calculate the total pressure acting on the drogue. By subtracting a reference pressure acting on the drogue (the pressure acting on the drogue calculated far

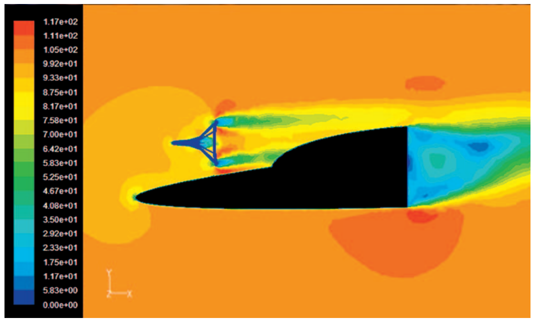

Fig. 13. Contours of velocity magnitude when $\boldsymbol{p}_{d/f} = [3.5, 0, 0]^{\mathrm{T}}$ (contour plot of velocity are level curves of velocity for position in CFD frame).

away from the receiver), the corresponding $\boldsymbol{f}_b$ is acquired. In this example, $\boldsymbol{f}_b = [82.5566, 0.20136833, 41.013971]^{\mathrm{T}}$.

Step 3. *Infer the form of* $\mathbf{F}_b(\cdot)$*:* The form of $\mathbf{F}_b(\cdot)$ is as follows:

$$\mathbf{F}_b(\boldsymbol{p}_d) = \begin{bmatrix} F_{bx}(\boldsymbol{p}_d) \\ F_{by}(\boldsymbol{p}_d) \\ F_{bz}(\boldsymbol{p}_d) \end{bmatrix} = \begin{bmatrix} f_{bx} \\ f_{by} \\ f_{bz} \end{bmatrix} = \begin{bmatrix} f_{bx\_nose} + f_{bx\_cockpit} \\ f_{by} \\ f_{bz} \end{bmatrix}. \tag{18}$$

Here,

$$\begin{cases} f_{bx\_nose} &= C_{x1}\left[1 - C_{x2}(x_d - C_{x3})^2\right] \\ & \quad \cdot e^{\frac{-y_d^2}{C_{x4}}} e^{\frac{z_d}{C_{x5}}} s\left(\frac{1}{\sqrt{C_{x2}}} + C_{x3} - x_d\right) \\ f_{bx\_cockpit} &= C_{x6}\left[1 - C_{x7}x_d\right] e^{\frac{-y_d^2}{C_{x8}}} e^{\frac{z_d}{C_{x9}}} \\ & \quad \cdot s\left(\frac{1}{C_{x7}} - x_d\right) \\ f_{by} &= C_{y1}\left(1 - C_{y2}x_d\right) y_d e^{\frac{-y_d^2}{C_{y3}}} e^{\frac{z_d}{C_{y4}}} \\ & \quad \cdot s\left(\frac{1}{C_{y2}} - x_d\right) \\ f_{bz} &= -C_{z1}\left(1 - C_{z2}x_d\right) e^{\frac{-y_d^2}{C_{z3}}} e^{\frac{z_d}{C_{z4}}} \\ & \quad \cdot s\left(\frac{1}{C_{z2}} - x_d\right) \end{cases}, \tag{19}$$

where $C_{(\cdot)} > 0$ denotes a parameter, and $s(\cdot)$ is defined in (14). The process to obtain (18) is illustrated as follows.

By plotting the training data, the profiles of $\boldsymbol{f}_b$ in different views are available, and these profiles are used to infer the forms of the functions. An example on deriving the concrete forms of F_{bz} is employed to explain the process. Fig. 14 shows three profiles of F_{bz}. First, the relations between F_{bz} and x_d, y_d, z_d are inferred from Fig. 14 (a), (b), (c), respectively, and they are expressed by $h_x(x_d)$, $h_y(y_d)$, $h_z(z_d)$: 1) the curves in Fig. 14(a) approximate to lines, but the force of the bow wave must not be negative, so $h_x(x_d)$ is expressed as $(1 - C_{z2}x_d) \cdot s\left(\frac{1}{C_{z2}} - x_d\right)$; 2) the curves in Fig. 14(b) are similar to normal distribution curves, so $h_y(y_d)$ is expressed as $e^{\frac{-y_d^2}{C_{z3}}}$; 3) similarly, the curves in Fig. 14(c) are expressed by $e^{\frac{z_d}{C_{z4}}}$. Second, the basic form of F_{bz} is assumed as $F_{bz}(x_d, y_d, z_d) = -C_{z1} \cdot h_x(x_d)\, h_y(y_d)\, h_z(z_d)$. Then, the parameters will be optimized by nonlinear regression in step 4, and the regression performance will be verified in step 5. If the obtained function cannot fit f_{bz} well, return to step 3 and change the parameterized functions. Finally, the form of F_{bz} is confirmed as (19) shown.

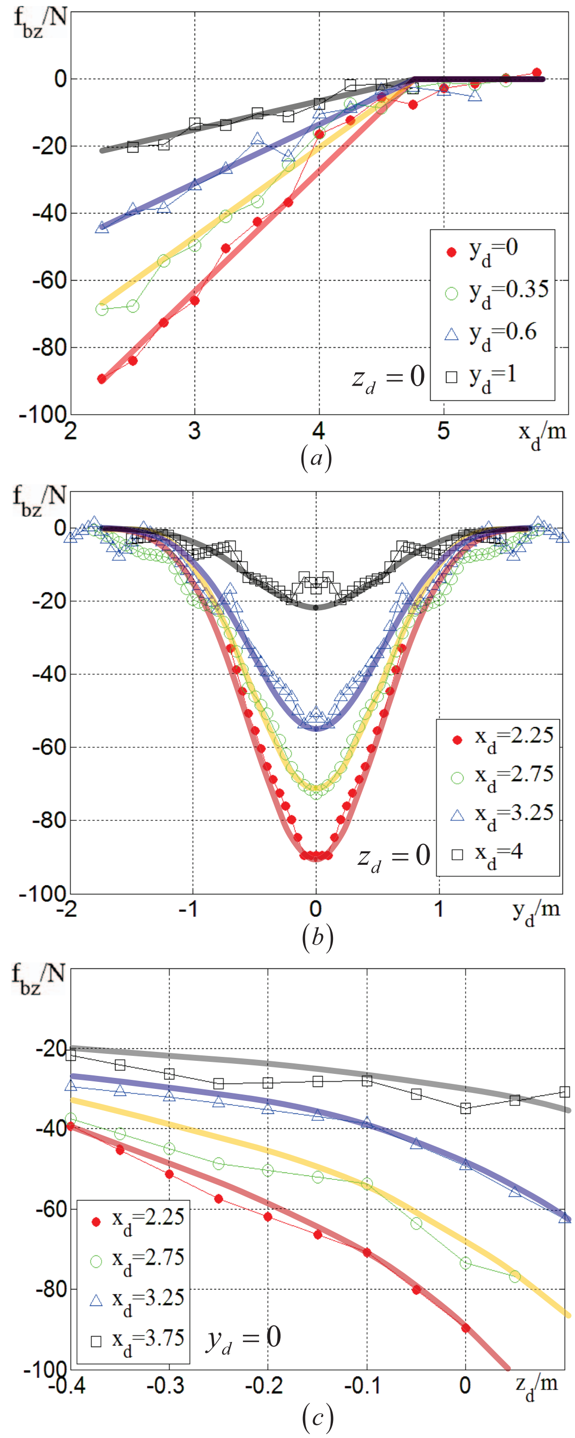

Fig. 14. Three profiles of F_{bz}.

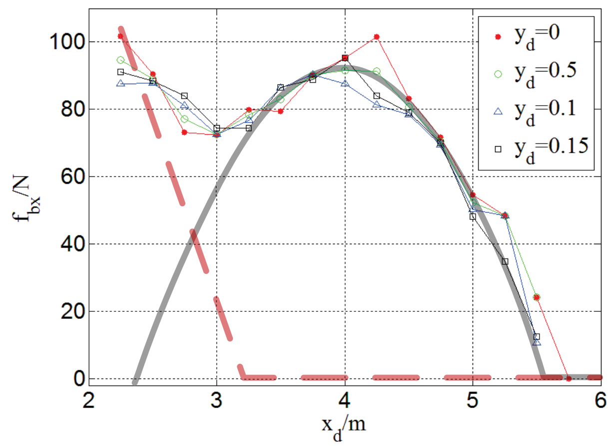

Fig. 15. Two components of F_{bx}: full line caused by nose and dash line caused by cockpit.

The forms of F_{bx} and F_{by} are obtained by the similar process. However, there is something different for F_{bx}. Fig. 15 shows that F_{bx} consists of two components: the force caused by the nose (full line) and the force caused by the cockpit (dash line). They work together to produce f_{bx}. Thus, F_{bx} is expressed by two functions as (18) shows and each of them is obtained by using the above process.

REMARK 5 The forms of F_{by} and F_{bz} are not decomposed into two parts in the considered area mentioned in remark 3. According to (13), the scope of the longitudinal force is further than those of the other two directions. Thus, in this area, the longitudinal force caused by the cockpit can be observed in this area. Meanwhile, in this area, the cockpit cannot influence the forces of the other two directions. This implies that they are influenced only by the nose. So, they do not have to be decomposed into two parts in this area. If these forces are considered in a larger area (for example the area behind the cockpit), then they will also be decomposed into two parts as the same as the longitudinal force.

Step 4. *Estimate the parameters of* $\mathbf{F}_b(\cdot)$*:* All of the training data are employed to estimate the parameters in (18). By taking $f_{bz} = F_{bz}(\boldsymbol{p}_d)$ as an example, $F_{bz}(\boldsymbol{p}_d)$ is rewritten to be $F_{bz}(\boldsymbol{p}_d, \boldsymbol{C}_z)$, where $\boldsymbol{C}_z = [C_{z1},\ C_{z2}, C_{z3}, C_{z4}]^{\mathrm{T}} \in \mathbb{R}_+^4$ are the undetermined parameters. The optimization problem to find $\boldsymbol{C}_z$ is formulated as follows:

$$\boldsymbol{C}_z^* = \underset{\boldsymbol{C}_z \in \mathbb{R}_+^4}{\arg\min} \sum_{k=1}^{N} \left[f_{bz,k} - F_{bz}\left(\boldsymbol{p}_{d,k}, \boldsymbol{C}_z\right)\right]^2, \qquad (20)$$

where N is the number of the training data. The constraint is that all the elements of $\boldsymbol{C}_z$ are positive. The initial value of $\boldsymbol{C}_z$ is chosen as $[170, 0.2, 0.5, 0.6]^{\mathrm{T}}$, which is estimated by curve fitting in the profiles. As a result, $F_{bz}(\boldsymbol{p}_d) = F'_{bz}(\boldsymbol{p}_d, \boldsymbol{C}_z^*)$. Similarly, the other parameters in (18) are determined. The results are shown in (13).

Step 5. *Check regression performance:* To check the regression performance, the coefficient of determination of the regression index R^2 is employed [26]. By taking f_{bz} as an example, it follows:

$$\begin{cases} SSE_z = \sum_{k=1}^{N} \left(f_{bz,k} - F_{bz}\left(\boldsymbol{p}_{d,k}, \boldsymbol{C}_z^*\right)\right)^2 \\ SST_z = \sum_{k=1}^{N} \left(f_{bz,k} - \frac{1}{N}\sum_{k=1}^{N} f_{bz,k}\right)^2 \end{cases}, \qquad (21)$$

and $R_z^2 = 1 - \frac{SSE_z}{SST_z}$. By using the training data, $R_x^2 = 0.8866,\ R_y^2 = 0.9536,\ R_z^2 = 0.9671$. In general, if $R^2 > 0.7$, then the regression performance is satisfied. Therefore, it is concluded that the obtained $\mathbf{F}_b(\cdot)$ approximates the bow wave force nicely.

REFERENCES

[1] Thomas, P. R., Bhandari, U., Bullock, S., Richardson, T. S., and du Bois, J. L.
Advances in air to air refueling.
Progress in Aerospace Sciences, **71** (2014), 14–35, DOI: 10.1016/j.paerosci.2014.07.001.

[2] Nalepka, J. P., and Hinchman, J. L.
Automated aerial refueling: Extending the effectiveness of unmanned air vehicles.
In *AIAA Modeling and Simulation Technologies Conference and Exhibit*, San Francisco, CA, Aug. 2005, AIAA Paper 2005–6005.

[3] Bhandari, U., Thomas, P. R., Bullock, S., Richardson, T. S., and du Bois, J. K.
Bow wave effect in probe-and-drogue aerial refuelling.
In *AIAA Guidance, Navigation, and Control Conference*, Boston, MA, Aug. 2013, AIAA Paper 2013-4695.

[4] Dogan, A., and Blake, W.
Modeling of bow wave effect in aerial refueling.
In *AIAA Atmospheric Flight Mechanics Conference*, Toronto, Ontario, Canada, Aug. 2010, AIAA Paper 2010-7926.

[5] NATO ATP-56(B) air-to-air refuelling. Tech. report, NATO, 2010.

[6] Campa, G., Napolitano, M. R., and Fravolini, M. L.
Simulation environment for machine vision based aerial refueling for UAVs.
IEEE Transactions on Aerospace and Electronic Systems, **71**, 1 (2009), 138–151, DOI: 10.1109/TAES.2009.4805269.

[7] Khansari-Zadeh, S. M., and Saghafi, F.
Vision-based navigation in autonomous close proximity operations using neural networks.
IEEE Transactions on Aerospace and Electronic Systems, **47**, 2 (2011), 864–883, DOI: 10.1109/TAES.2011.5751231.

[8] Hansen, J. L., Murray, J. E., and Campos, N. V.
The NASA Dryden AAR project: A flight test approach to an aerial refueling system.
In *AIAA Atmospheric Flight Mechanics Conference and Exhibit*, Providence, RI, Aug. 2004, AIAA Paper 2004-4939.

[9] Dibley, R. P., Allen, M. J., and Nabaa, N.
Autonomous airborne refueling demonstration phase I flight-test results.
In *AIAA Atmospheric Flight Mechanics Conference and Exhibit*, Hilton Head, SC, Aug. 2007, AIAA Paper 2007-6639.

[10] Ro, K., Kuk, T., and Kamman, J. W.
Active control of aerial refueling hose-drogue systems.
In *AIAA Guidance, Navigation, and Control Conference*, Toronto, Ontario, Canada, Aug. 2010, AIAA Paper 2010-8400.

[11] Dogan, A., Blake, W., and Haag, C.
Bow wave effect in aerial refueling: Computational analysis and modeling
Journal of Aircraft, **50**, 6 (2013), 1856–1868, DOI: 10.2514/1.C032165.

[12] Khan, O., and Masud, J.

Trajectory analysis of basket engagement during aerial refueling.
In *AIAA Atmospheric Flight Mechanics Conference*, 2014, AIAA Paper 2014-0190.

[13] Ro, K., and Kamman J. W.
Modeling and simulation of hose-paradrogue aerial refueling systems.
Journal of Guidance, Control, and Dynamics, **33**, 1 (2010), 53–63, DOI: 10.2514/1.45482.

[14] Wei, Z.-B., Quan, Q., and Cai, K.-Y.
Research on relation between drogue position and interference force for probe-drogue aerial refueling system based on link-connected model.
The 31st Chinese Control Conference, Hefei, China, July 2012, 1777–1782 (in Chinese).

[15] Stevens, B. L., and Lewis, F. L.
Aircraft Control and Simulation, 2nd ed. New York: Wiley, 2003, pp. 4–5.

[16] Dogan, A., Timothy L., and William B.
Wake-vortex induced wind with turbulence in aerial refueling—Part A: Flight data analysis.
In *AIAA Atmospheric Flight Mechanics Conference and Exhibit*, Honolulu, HI, Aug. 2008, AIAA Paper 2008-6696.

[17] Dogan, A., Timothy L., and William B.
Wake-vortex induced wind with turbulence in aerial refueling—Part B: Model and simulation validation.
In *AIAA Atmospheric Flight Mechanics Conference and Exhibit*, Honolulu, HI, Aug. 2008, AIAA Paper 2008-6697.

[18] Venkataramanan, S., and Dogan, A.
Dynamic effect of trailing vortex with turbulence & time-varying inertia in aerial refueling.
In *AIAA Atmospheric Flight Mechanics Conference and Exhibit*, Providence, RI, Aug. 2004, AIAA Paper 2004-4945.

[19] Fravolini, M. L., Ficola, A., Napolitano, M. R., Campa G., and Perhinschi, M. G.
Development of modeling and control tools for aerial refueling for UAVs.
In *AIAA Guidance, Navigation, and Control Conference and Exhibit*, Austin, TX, Aug. 2003, AIAA Paper 2003-5798.

[20] Tandale, M. D., Bowers, R., and Valasek, J.
Trajectory tracking controller for vision-based probe-and-drogue autonomous aerial refueling.
Journal of Guidance, Control, and Dynamics, **29**, 4 (2006), 846–857, DOI: 10.2514/1.19694.

[21] Ro, K., Basaran, E., and Kamman, J. W.
Aerodynamic characteristics of paradrogue assembly in an aerial refueling system.
Journal of Aircraft, **44**, 3 (2007), 963–970, DOI: 10.2514/1.26489.

[22] The drogue dynamics under receiver's bow wave. Available: http://youtu.be/xkWkAlfhUX0.

[23] Vassberg, J. C., Yeh, D. T., Blair, A. J., and Evert, J. M.
Numerical simulations of KC-10 wing-mount aerial refueling hose-drogue dynamics with a reel take-up system.
In *21st Applied Aerodynamics Conference*, Orlando, FL, June 2003, AIAA Paper 2003-3508.

[24] Klein, V., and Morelli, E. A.
Aircraft System Identification: Theory and Practice. Reston, VA: AIAA, 2006,
pp. 395–399.

[25] Wei, Z.-B., Dai, X., Quan, Q., and Cai, K.-Y.
Dataset and analysis of bow wave effect based on Fluent. Available: http://rfly.buaa.edu.cn/resources/ #DatasetBowWaveCFD.

[26] Weisberg, S.
Applied Linear Regression, 4th ed. NewYork: Wiley, 2005, pp. 33–35.

Zi-Bo Wei is a Ph.D. candidate of School of Automation Science and Electrical Engineering at Beihang University (Beijing University of Aeronautics and Astronautics), Beijing, China. His main research interests are aerial refueling, iterative learning control, and accurate flight control.

Xunhua Dai received the B.S. and M.S. degrees from School of Automation Science and Electrical Engineering, Beihang University, Beijing, China, in 2013 and 2016, respectively. His main research interests are aerial refueling and flying control.

Quan Quan received the B.S. and Ph.D. degrees from Beihang University, Beijing, China, in 2004 and 2010, respectively.

He has been an associate professor in Beihang University since 2013. His main research interests include vision-based navigation and reliable flight control.

Kai-Yuan Cai received the B.S., M.S., and Ph.D. degrees from Beihang University, Beijing, China, in 1984, 1987, and 1991, respectively. He has been a full professor at Beihang University since 1995. He is a Cheung Kong Scholar (chair professor), jointly appointed by the Ministry of Education of China and the Li Ka Shing Foundation of Hong Kong in 1999. His main research interests include software testing, software reliability, reliable flight control, and software cybernetics.